Scilight

Smart Materials and Devices
https://www.sciltp.com/journals/smd

Article

Microstructural Evolution and Twinning Mechanism in Cold-Drawn CoNiV Medium-Entropy Alloy

Lin Deng [1], Jinru Luo [2,3,*], Rongzhi Li [1] and Yong Zhang [1,4,*]

[1] State Key Laboratory for Advanced Metals and Materials, University of Science and Technology Beijing, Beijing 100083, China
[2] Department of Ferrous Metallurgy, University of Science and Technology Beijing, Beijing 100083, China
[3] JITRI Advanced Materials R&D Co. Ltd., Yangtze Delta, Suzhou 215133, China
[4] Key Laboratory of Silicon-Based Materials, Fuyao University of Science and Technology, Fuzhou 350109, China
* Correspondence: luojinru@ustb.edu.cn (J.L.); yongzhang@fyust.edu.cn (Y.Z.)

How To Cite: Deng, L.; Luo, J.; Li, R.; et al. Microstructural Evolution and Twinning Mechanism in Cold-Drawn CoNiV Medium-Entropy Alloy. *Smart Materials and Devices* **2025**, *1*(1), 2.

Received: 23 May 2025
Revised: 19 June 2025
Accepted: 8 July 2025
Published: 10 July 2025

Abstract: The microstructural evolution of a CoNiV medium-entropy alloy (MEA) during cold drawing was investigated. The alloy maintains a single-phase FCC structure, with annealing twins in the as-annealed state and deformation twins forming after drawing. Despite its high stacking fault energy, the applied drawing stress (2410 MPa) exceeds the critical twinning stress (1903 MPa), enabling deformation twinning. No 9R phase was observed, which is attributed to its thermodynamic instability, as confirmed by first-principles calculations. These findings clarify the deformation behavior and twin formation mechanism in CoNiV MEAs under severe plastic deformation.

Keywords: CoNiV; medium-entropy alloy; deformation twins; 9R

1. Introduction

Medium-entropy alloys (MEAs) can be regarded as the core subset in the high entropy alloys (HEAs), e.g., CoNiV in the CoNiVAlTi [1], TiZrNb in the TiZrNbMoV [2], CoCrNi in the CoCrFeMnMNi [3], etc. MEAs have emerged as a new class of structural materials due to their exceptional properties, including high strength, excellent ductility, corrosion resistance, and irradiation tolerance [4–10]. Among them, the CoNiV MEA exhibits superior yield strength and ductility compared to most quaternary and quinary systems [11,12]. To date, the mechanical performance of CoNiV MEAs has been enhanced through conventional mechanisms such as solid solution strengthening, grain refinement, dislocation strengthening, and second-phase reinforcement [13,14]. The reported optimized mechanical properties include strengths exceeding 2 GPa and fracture strains approaching 20% [15]. Further improvements in strength–ductility synergy rely on the activation of additional deformation mechanisms to sustain high work-hardening capability during plastic deformation; otherwise, premature necking will occur due to insufficient strain hardening [13,16–19]. Among various nano defects, deformation twins (DTs) and 9R phase are effective barriers for dislocation motion within grains, thereby enhancing both the strength and strain hardening capacity of alloys [20]. However, due to the relatively high stacking fault energy (SFE) of the CoNiV MEA, plastic deformation is primarily governed by dislocation slip, and neither DTs nor 9R structures have been observed—even at cryogenic temperatures [21]. Fortunately, increasing the local flow stress makes the formation of DTs and 9R phases more feasible, a phenomenon that has been extensively demonstrated in high-SFE metals such as pure aluminum [22]. In this study, cold drawing was employed to raise the flow stress of CoNiV MEA and to investigate the potential formation of DTs and 9R phases under high-stress conditions.

Copyright: © 2025 by the authors. This is an open access article under the terms and conditions of the Creative Commons Attribution (CC BY) license (https://creativecommons.org/licenses/by/4.0/).
Publisher's Note: Scilight stays neutral with regard to jurisdictional claims in published maps and institutional affiliations.

2. Experimental Procedures

2.1. Alloy Preparation

A master HEA with a nominal composition of $Co_{33.34}Ni_{33.33}V_{33.33}$ (at.%) was prepared by vacuum arc melting under a high-purity argon atmosphere, followed by suction casting into a rectangular ingot with dimensions of 10 × 10 × 50 mm. To ensure compositional homogeneity, the alloy was remelted four times. The ingot was homogenized at 1000 °C for 30 min, hot-rolled at the same temperature to a thickness of 6 mm by a hot rolling mill equipped with a heating furnace, and then air-cooled. Subsequently, the alloy was homogenized again at 1000 °C for 2 h and water-quenched. The sample was further cold-rolled to a thickness of 1 mm and annealed at 1000 °C for 10 min, followed by water quenching. Both hot and cold rolling were performed with a 1 mm reduction per pass. Samples were cut into 1 × 1 × 200 mm specimens using electrical discharge machining for subsequent cold drawing. The wire diameter was reduced by 100 μm in each drawing step until reaching a final diameter of 300 μm.

2.2. Microstructure and Mechanical Properties

Microstructural characterization was performed using a field emission scanning electron microscope (FE-SEM, Aztec Max2, Oxford Nordlys, UK) equipped with backscattered electron imaging (BSEI). Transmission electron microscopy (TEM), selected area electron diffraction (SAED), and high-resolution TEM (HRTEM) analyses were conducted using a field emission gun TEM (FEG-TEM, Tecnai G2 F20, FEI Company, Hillsboro, OR, USA). For SEM, samples were ground to 5000# and electropolished at −20 °C in a solution of 10% $HClO_4$ and 90% C_2H_5OH for 1 min. TEM foils were thinned to <100 nm at 100 K using ion-beam. Prior to ion milling, the specimens were mechanically ground to a thickness of approximately 40 μm. X-ray diffraction (XRD) analysis was conducted using an in-situ XRD system (NANOPIX-WE, Rigaku, Japan) with a Mo Kα radiation source (λ = 0.071 nm). Quasi-static uniaxial tensile tests were performed at room temperature using a material testing system (MTS) at a strain rate of 1×10^{-3} s^{-1}. The tensile specimens were 40 mm in length.

2.3. First-Principles Method

First-principles calculations were performed using the Vienna Ab initio Simulation Package (VASP) to determine the cohesive energies of FCC, FCC/9R, and 9R structures in the CoNiV alloy. The supercell for the geometrically optimized FCC structure contained 120 atoms (dimensions: 8.7 × 30.9 × 5.5) randomly distributed across the lattice sites of the corresponding crystal structure. The exchange-correlation functional was modeled using the generalized gradient approximation (GGA) with the Perdew-Burke-Ernzerhof (PBE) functional, and ultrasoft pseudopotentials (USPP) were utilized to describe electron-ion interactions. The calculation parameters included a plane-wave energy cutoff of 310 eV, a k-point grid of 3 × 2 × 1, and an error threshold of 1.0×10^{-6} eV/Atom. The convergence criteria for SCF iterations required that the total energy difference between two consecutive cycles be less than 5.0×10^{-6} eV/atom, with a tolerance offset of less than 5.0×10^{-5} nm.

3. Results and Discussion

As shown in Figure 1a, the XRD pattern indicates that the CoNiV MEA primarily exhibits a single-phase FCC structure, and no new phases are generated during cold drawing. Figure 1b displays the SEM image of the as-annealed CoNiV MEA, revealing equiaxed grains with an average size of 4.4 ± 2.7 μm. A large number of twins are observed within the grains. Due to their relatively large thickness, these twins are identified as annealing twins (ATs), likely formed during the annealing process as a result of grain boundary energy reduction [23]. The EDS results shown in Figure 1d–f confirm that the elemental distribution in the CoNiV alloy is uniform, with no detectable elemental segregation. After cold drawing, the grains are fragmented, and finer twins emerge, displaying parallel stripe-like features extending from grain boundaries into the grain interiors (Figure 1c). These features are considered deformation twins (DTs) formed during cold drawing [23]. Although the CoNiV MEA has a high stacking fault energy, the elevated flow stress induced by cold drawing surpasses the critical twinning stress, thereby promoting the formation of DTs, which will be discussed in detail later.

Shear stress can trigger the formation of the 9R phase via Σ3 {112} twin boundary dissociation or periodic Shockley partial emission on {111} planes. [24]. Additionally, the 9R phase can serve as a nucleation core for DTs, hexagonal close-packed (HCP) structures, and σ phases, and has been widely observed in FCC alloys [20,24]. Therefore, the twin regions of the CoNiV MEA before and after cold drawing were carefully examined, as shown in Figure 2. Before cold drawing, a high density of ATs appeared within individual grains (Figure 2a,b), with

widths ranging from 15 nm to 150 nm. Figure 2b$_1$ shows the symmetrical structure of the twins. As the degree of cold drawing increases (i.e., with decreasing wire diameter), the grains become significantly elongated and gradually refined. In the early stages of deformation (e.g., at a diameter of D = 0.8 μm, Figure 2c), well-defined dislocation cell (DC) structures can still be observed. However, with further drawing, the microstructure progressively evolves into one dominated by microbands (MBs, Figure 2d–f). Notably, the formation of deformation twins (DTs) appears to have a critical size threshold: prominent DTs are only observed when the diameter is reduced to approximately 0.4 μm (Figure 2e), with an average twin thickness of ~10 nm. Upon further reduction in diameter to 0.3 μm (Figure 2f), the volume fraction of deformation twins increases significantly. Surprisingly, despite being subjected to extremely high stress, the area surrounding the DTs remains remarkably "clean", with no 9R phases detected (Figure 2g$_1$).

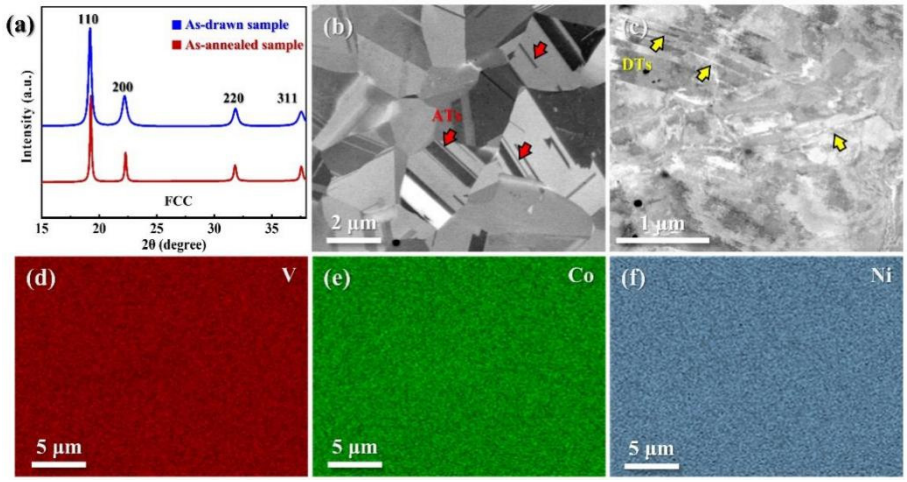

Figure 1. (**a**) XRD pattern of CoNiV MEAs before and after drawing; ECCI images of the CoNiV MEA in the (**b**) as-annealed and (**c**) as-drawn states; (**d**–**f**) EDS maps of the as-annealed CoNiV MEA.

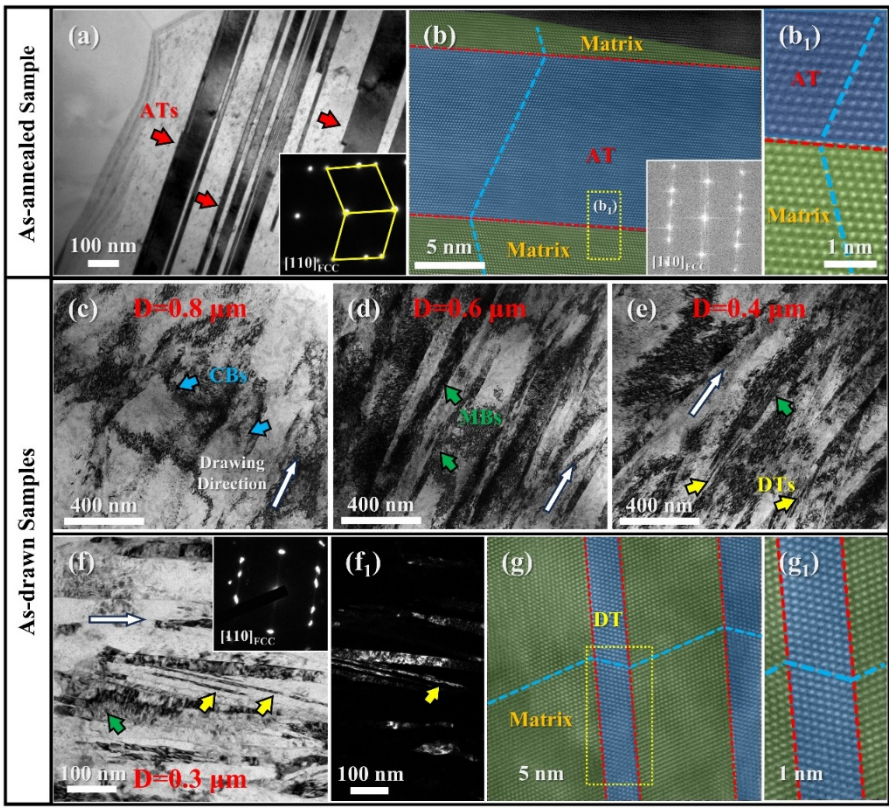

Figure 2. (**a**) TEM image and the corresponding SAED pattern of ATs in the as-annealed CoNiV alloy; (**b**) HRTEM image shows the ATs and their magnified view in (**b$_1$**); (**c**–**f**) TEM images show the microstructural evolution of the CoNiV MEA under varying degrees of cold drawing: (**c**) 0.8 μm, (**d**) 0.6 μm, (**e**) 0.4 μm, and (**f**) 0.3 μm; (**f$_1$**) corresponding dark-field TEM image of (**f**); (**g**) HRTEM image of DTs in (**f**) and their magnified view in (**g$_1$**).

Although the CoNiV MEA has a higher stacking fault energy than typical H/MEAs, it is worth noting that the 9R phase has been observed even in Al alloys with extremely high stacking fault energies (166 mJ/m²) under severe shear stress [22]. The occurrence of stress-induced phase transformation requires both thermodynamic and kinetic feasibility [25]. Thermodynamically, a negative Gibbs free energy difference ($\Delta G < 0$) between the two phases is essential to provide the necessary driving force for the transformation. Kinetically, the applied stress must exceed a critical transformation stress to supply sufficient mechanical energy to overcome the transformation energy barrier, thereby enabling the phase change. To elucidate why the 9R structure is difficult to form in the CoNiV MEA, first-principles calculations were performed to determine the cohesive energies of the FCC, 9R, and 9R/FCC structures in CoNiV MEA. In general, more negative cohesive energy indicates a higher energy release during atomic bonding, leading to stronger interatomic bonds and a more stable structure. The cohesive energy was calculated using the following equation [26]:

$$E_{coh} = E^{AB}{}_{total} - (cE^{A}{}_{atom} + (1 - c)E^{B}{}_{atom}) \quad (1)$$

where E_{coh} represents the cohesive energy; E_{total} and E_{atom} denote the energy of the alloy and the single atom in the cell dot matrix of the alloy, respectively; c represents the fraction of the different atoms. The computational results, depicted in Figure 3b, show that the 9R structure in CoNiV alloys has the highest cohesive energy, followed by the 9R/FCC interface, while the FCC phase exhibits the lowest cohesive energy. These results indicate that the FCC phase is the thermodynamically stable structure in the CoNiV MEA, and the formation of either the 9R phase or the 9R/FCC interface within the matrix is energetically unfavorable. In contrast, in some HEAs with low stacking fault energies, the 9R phase and 9R/FCC interfaces are more stable than the FCC phase [24]. As a result, the metastable FCC structure in such alloys tends to transform into the 9R structure upon deformation.

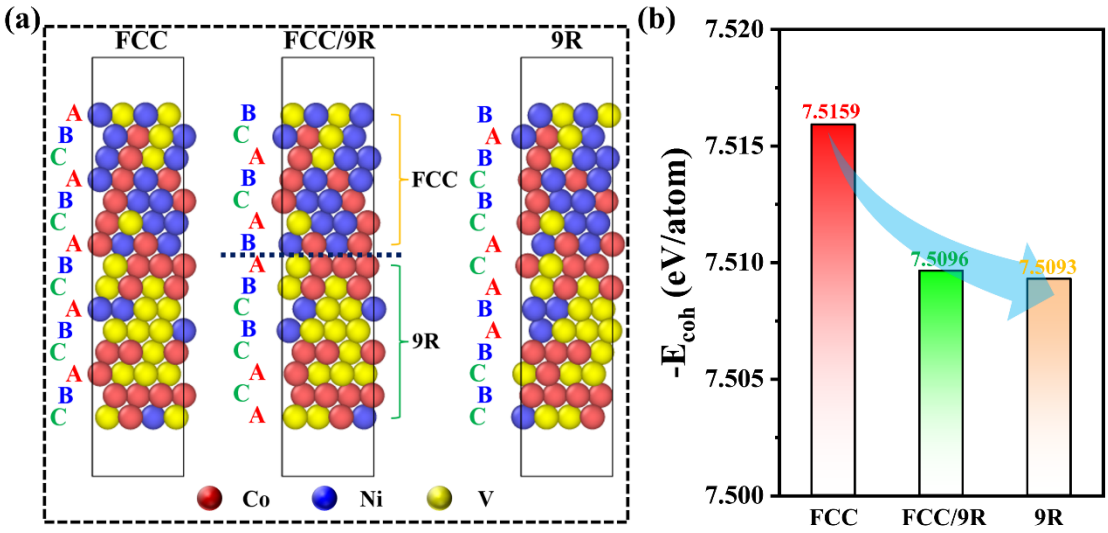

Figure 3. (**a**) The atomic configurations of the original FCC, FCC/9R, and 9R structures; (**b**) First-principles calculated cohesive energy of FCC, FCC/9R, and 9R structures in the CoNiV alloy.

Apart from the 9R phase, DTs have also rarely been observed in single-phase CoNiV MEAs in previous studies. However, in the present study, DTs were successfully introduced through cold drawing, indicating the activation of a new deformation mechanism. In materials with an FCC crystal structure, the activation of deformation twinning requires the applied stress to exceed the critical twinning stress, thereby satisfying the kinetic conditions for twinning. The magnitude of the critical twinning stress is strongly influenced by both grain size and SFE; finer grains and higher SFE lead to higher critical twinning stresses, making the activation of twinning more difficult. It has been reported that the critical twinning stress in alloys can be estimated using the following equation [13]:

$$\tau_{tw} = M\left(\frac{\gamma}{b_p} + \frac{k_{tw}^{H\text{-}P}}{d}\right) \quad (2)$$

where γ is the SFE (31 mJ/m^2 for CoNiV MEA), M is the Talyor factor (3.06 for CoNiV MEA), b_p is the Burger's vector of a partial dislocation (0.147 nm), $k_{tw}^{H\text{-}P}$ is Hall-Petch constant for twinning (864 MPa μm$^{1/2}$ for CoNiV MEA [27]), d represents the mean grain size. The calculated critical twinning stress of the as-annealed CoNiV MEA in this study reaches 1903 MPa, which explains why DTs were rarely observed in previous uniaxial

tensile experiments. Generally, severe plastic deformation methods such as cold drawing can provide higher flow stress than uniaxial tension, thereby facilitating the activation of DTs. The equivalent stress during cold drawing can be calculated using the following equations [28]:

$$\frac{\sigma_f}{\sigma_0} = ln\left(\frac{R_i}{R_f}\right) + \mu cot\alpha\, ln\left(\frac{R_i}{R_f}\right) + \frac{2\alpha}{3} \tag{3}$$

where σ_f represents the effective drawing stress, σ_0 represents the yield stress (1.7 GPa, show in Figure 4), R_i and R_f are the wire radii before and after passing through the die (0.2 mm → 0.15 mm), respectively, α represent the die semi-angle (3° in this study), and μ is the friction coefficient (0.2 in this study). The calculated effective drawing stress is 2410 MPa, which exceeds the critical stress required for deformation twinning (Figure 4), thereby inducing a high density of DTs in the matrix. Another noteworthy point is that, despite the presence of high local stress during cold drawing, the 9R phase transformation does not occur because the thermodynamic conditions required for its activation are not met, as confirmed by our earlier first-principles calculations.

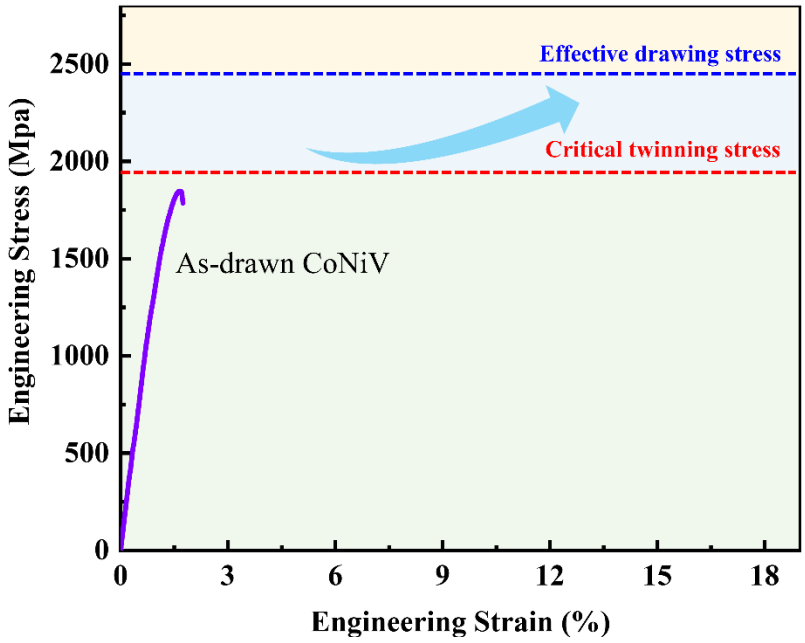

Figure 4. Comparison of the engineering stress–strain curve with the critical twinning stress and the effective drawing stress.

4. Conclusions

In summary, this study investigated the microstructural evolution and deformation mechanisms of a CoNiV medium-entropy alloy (MEA) during cold drawing. The alloy retains a single-phase FCC structure throughout deformation. Cold drawing transforms ATs into ultrafine DTs, enabled by a drawing stress (2410 MPa) that exceeds the critical twinning stress (1903 MPa), despite the alloy's high stacking fault energy. No 9R phase forms, which is attributed to its thermodynamic instability, as revealed by first-principles cohesive energy calculations. These findings highlight the roles of stacking fault energy, grain size, and deformation stress in controlling twin formation and phase stability in high-strength MEAs.

Author Contributions

L.D.: Writing—original draft, visualization, methodology, formal analysis, data curation; J.L.: Writing—review & editing, supervision, resources, funding acquisition; R.L.: writing—reviewing and editing; Y.Z.: Writing—review and editing, supervision, project administration, methodology, funding acquisition, conceptualization. All authors have read and agreed to the published version of the manuscript.

Funding

Financial support from the National Natural Science Foundation of China (52371165 and 12275237), the Department of Science and Technology of Fuzhou city (2024-Y-017, 2024-SG-003 and 2024-SG-004), the Key Laboratory of Silicon-based Materials, The Ministry of Education, P. R. China, the Key Laboratory of Silicon-

based Materials, The Ministry of Education, P. R. China, the Key Laboratory of Automotive Glass of Fujian, the Smart Automotive Glass Engineering Research Center of Fujian, the Space Application System of China Manned Space Program (KJZ-YY-NCL09) and China-ESA international cooperation (KF-2020-68) are gratefully acknowledged.

Institutional Review Board Statement

The study did not involve human participants or animal experiments. Therefore, ethical review and approval were waived for this research.

Informed Consent Statement

Not applicable. This study did not involve human participants.

Data Availability Statement

The datasets generated and analyzed during the current study are available from the corresponding author upon reasonable request. The data will be retained for at least 10 years following publication through institutional archives or subject-specific repositories, with access restrictions applied only to protect participant confidentiality or proprietary rights.

Conflicts of Interest

The authors declare no conflict of interest. The funders had no role in the design of the study; in the collection, analyses, or interpretation of data; in the writing of the manuscript; or in the decision to publish the results.

References

1. Li, Y.; Liao, W.-B.; Chen, H.; et al. A low-density high-entropy dual-phase alloy with hierarchical structure and exceptional specific yield strength. *Sci. China Mater.* **2023**, *66*, 780–792.
2. Wu, Y.D.; Cai, Y.H.; Chen, X.H.; et al. Phase composition and solid solution strengthening effect in TiZrNbMoV high-entropy alloys. *Mater. Des.* **2015**, *83*, 651–660.
3. Cantor, B.; Chang, I.T.H.; Knight, P.; et al. Microstructural development in equiatomic multicomponent alloys. *Mater. Sci. Eng. A* **2004**, *375*, 213–218.
4. Deng, L.; Li, R.; Luo, J.; et al. Plastic deformation and strengthening mechanism in CoNiV medium-entropy alloy fiber. *Int. J. Plast.* **2024**, *175*, 103929.
5. Fu, Y.; Li, J.; Luo, H.; et al. Recent advances on environmental corrosion behavior and mechanism of high-entropy alloys. *J. Mater. Sci. Technol.* **2021**, *80*, 217–233.
6. Chen, Y.; Wang, S.; Feng, H.; et al. Irradiation hardening behavior of high entropy alloys using random field theory informed discrete dislocation dynamics simulation. *Int. J. Plast.* **2023**, *162*, 103497.
7. Deng, L.; Bai, C.-Y.; Jiang, Z.-T.; et al. Effect of B4C particles addition on microstructure and mechanical properties of $Fe_{50}Mn_{30}Co_{10}Cr_{10}$ high-entropy alloy. *Mater. Sci. Eng. A* **2021**, *822*, 141642. https://doi.org/10.1016/j.msea.2021.141642.
8. Li, R.; Liaw, P.K.; Jiang, J.; et al. Advanced Applications for Smart-Metallic Materials. *Smart Mater. Devices* **2025**, *1*, 100001.
9. Bai, C.; Tu, J.; Yang, L.; et al. Synergistic enhancement of strength-ductility through multi-phase heterogeneous structure induced by SiC particle addition in CoCrFeNi high entropy alloy. *Mater. Sci. Eng. A* **2025**, *924*, 147753.
10. Yi, M.; Tu, J.; Yang, L.; et al. Microstructural mechanisms endowing high strength-ductility synergy in CoCrNi medium entropy alloy prepared by laser powder bed fusion. *Addit. Manuf.* **2024**, *87*, 104229. https://doi.org/10.1016/j.addma.2024.104229.
11. Amar, A.; Wang, M.; Huang, R.; et al. Ultra-strong and ductile medium entropy alloy with a dual heterogeneous microstructure. *Acta Mater.* **2024**, *284*, 120645.
12. Cai, W.; Long, Q.; Lu, S.; et al. Enhanced strength-ductility synergy in medium entropy alloy via phase selective precipitation. *Int. J. Plast.* **2025**, *184*, 104204. https://doi.org/10.1016/j.ijplas.2024.104204.
13. An, F.; Hou, J.; Liu, J.; et al. Deformable κ phase induced deformation twins in a CoNiV medium entropy alloy. *Int. J. Plast.* **2023**, *160*, 103509.
14. Xu, L.; Ma, Y.; Zhang, Z.; et al. Superior tensile properties induced by triple-level heterogeneous structures in the CoNiV-based medium-entropy alloy. *J. Mater. Sci. Technol.* **2025**, *214*, 245–254. https://doi.org/10.1016/j.jmst.2024.07.020.
15. Xu, B.; Duan, H.; Chen, X.; et al. Harnessing instability for work hardening in multi-principal element alloys. *Nat. Mater.* **2024**, *23*, 755–761.
16. Lee, B.J.; Shim, S.H.; Lee, H.B.; et al. Deformation-induced multi-step TRIP/TWIP (fcc, hcp) behaviors in metastable

Fe55Mn25Co10Cr10 high-entropy alloy at ambient and cryogenic temperatures. *Mater. Sci. Eng. A* **2024**, *913*, 147030.
17. Mu, Y.; Liang, Y.; Sheng, J.; et al. A novel approach to coating for improving the comprehensive high-temperature service performance of TiAl alloys. *Acta Mater.* **2025**, *283*, 120500.
18. Zhang, C.; Wang, R.; Pan, K.; et al. Preparation and enhanced oxidation behavior of microalloyed Mo_5SiB_2 alloy at 1300 °C. *Mater. Charact.* **2022**, *189*, 112001.
19. Deng, L.; Luo, J.-R.; Tu, J.; et al. Achieving excellent mechanical properties of ODS steel by Y_2O_3 addition. *Mater. Sci. Eng. A* **2023**, *872*, 145008.
20. Zhang, J.; Zhou, D.; Pang, X.; et al. Deformation-induced concurrent formation of 9R phase and twins in a nanograined aluminum alloy. *Acta Mater.* **2023**, *244*, 118540.
21. Nutor, R.K.; Xu, T.; Wang, X.; et al. Liquid helium temperature deformation and local atomic structure of CoNiV medium entropy alloy. *Mater. Today Commun.* **2022**, *30*, 103141.
22. Xue, S.; Fan, Z.; Lawal, O.B.; et al. High-velocity projectile impact induced 9R phase in ultrafine-grained aluminium. *Nat. Commun.* **2017**, *8*, 1653.
23. Zhang, Z.; Jiang, Z.; Xie, Y.; et al. Multiple deformation mechanisms induced by pre-twinning in CoCrFeNi high entropy alloy. *Scr. Mater.* **2022**, *207*, 114266.
24. Wang, L.X.; Xiang, S.; Tan, Y.B.; et al. The role of 9R structures on deformation-induced martensitic phase transformations in dual-phase high-entropy alloys. *Mater. Sci. Eng. A* **2022**, *853*, 143705.
25. Deng, L.; Luo, J.; Liang, Y.; et al. Synergistic increasing the Strength–Elasticity in a CoNiV medium-entropy alloy via cold drawing. *Mater. Sci. Eng. A* **2025**, *941*, 148577.
26. Sahu, B.R. Electronic structure and bonding of ultralight LiMg. *Mater. Sci. Eng. B* **1997**, *49*, 74–78.
27. Gutierrez-Urrutia, I.; Zaefferer, S.; Raabe, D. The effect of grain size and grain orientation on deformation twinning in a Fe–22 wt.% Mn–0.6 wt.% C TWIP steel. *Mater. Sci. Eng. A* **2010**, *527*, 3552–3560.
28. Vega, G.; Haddi, A.; Imad, A. Investigation of process parameters effect on the copper-wire drawing. *Mater. Des.* **2009**, *30*, 3308–3312.